CODE 6000
A. I. SCHINDLER

NRL Report 8418

Physical Limitations and Design Criteria for a Solid State Gyrotron

A.K. GANGULY AND D.C. WEBB

Microwave Technology Branch
Electronics Technology Division

October 24, 1980

NAVAL RESEARCH LABORATORY
Washington, D.C.

Approved for public release; distribution unlimited.

SECURITY CLASSIFICATION OF THIS PAGE *(When Data Entered)*

REPORT DOCUMENTATION PAGE		READ INSTRUCTIONS BEFORE COMPLETING FORM
1. REPORT NUMBER NRL Report 8418	2. GOVT ACCESSION NO.	3. RECIPIENT'S CATALOG NUMBER
4. TITLE *(and Subtitle)* PHYSICAL LIMITATIONS AND DESIGN CRITERIA FOR A SOLID-STATE GYROTRON		5. TYPE OF REPORT & PERIOD COVERED Interim report on a continuing NRL problem 6. PERFORMING ORG. REPORT NUMBER
7. AUTHOR(s) A.K. Ganguly and D.C. Webb		8. CONTRACT OR GRANT NUMBER(s)
9. PERFORMING ORGANIZATION NAME AND ADDRESS Naval Research Laboratory Washington, DC 20375		10. PROGRAM ELEMENT, PROJECT, TASK AREA & WORK UNIT NUMBERS NRL Problem 52-0791-0-0 Project RR 021-03-46
11. CONTROLLING OFFICE NAME AND ADDRESS Office of Naval Research Arlington, VA 22217		12. REPORT DATE October 24, 1980 13. NUMBER OF PAGES 20
14. MONITORING AGENCY NAME & ADDRESS*(if different from Controlling Office)*		15. SECURITY CLASS. *(of this report)* Unclassified 15a. DECLASSIFICATION/DOWNGRADING SCHEDULE

16. DISTRIBUTION STATEMENT *(of this Report)*

Approved for public release; distribution unlimited.

17. DISTRIBUTION STATEMENT *(of the abstract entered in Block 20, if different from Report)*

18. SUPPLEMENTARY NOTES

19. KEY WORDS *(Continue on reverse side if necessary and identify by block number)*

Submillimeter wave
Gyrotron
Oscillator
Indium antimonide

20. ABSTRACT *(Continue on reverse side if necessary and identify by block number)*

Scaling of conventional microwave sources to operate in the near millimeter wave (100–1000 GHz) portion of the electromagnetic spectrum is difficult and often impossible. Severe fabrication and heat dissipation problems are common. In the microwave tube area, workers at the Naval Research Laboratory and elsewhere have shown that the severity of these problems can be considerably reduced by employing the electromagnetically large gyrotron configuration, and kilowatts of

(Continued)

20. ABSTRACT (Continued)

continuous power have been generated at millimeter wavelengths. In this report we investigate the possibility of applying similar design principles to the development of solid-state gyrotron.

In this report we review the physical mechanism that gives rise to oscillations and present the underlying mathematics. Numerous nonideal factors are considered; namely, a finite electron mean-free-path, injection of electrons which are not monoenergetic, metallic and dielectric ohmic losses in the resonant cavity, and presence of a finite electric field in the interaction region. Use of a reverse-biased Schottky tunnel barrier for electron injection is analyzed in detail and is found to be a promising structure for producing sufficient current to sustain oscillations. Calculations are based on InSb parameters, as this material appears best for this application because of its long mean-free path. The main conclusions of this study are that (a) with available materials it is unlikely that oscillations can be sustained and (b) with three- to fivefold increase in the mean-free-path, oscillations appear possible, albeit at a very high frequency (~ 1000 GHz).

CONTENTS

PHYSICAL LIMITATIONS AND DESIGN CRITERIA FOR A SOLID STATE GYROTRON

INTRODUCTION

In a recent publication [1] the basic operating principles and a mathematical analysis of a new type of solid state source—the solid state gyrotron or cyclotron maser—were presented. In this device the energy to sustain oscillations is derived from a gyrating electron beam in a manner similar to the highly successful gyrotron tube [2]. In order that energy be transferred from the electron beam to the electromagnetic fields, a mechanism for bunching the electrons must exist. Unlike the gyrotron tube, which relies on relativistic effects to accomplish the bunching, the solid state version relies on the nonparabolic conduction band of certain semiconductors, e.g., InSb. The frequency of operation depends on the ratio of magnetic bias field to the effective electron mass m^*. For InSb, m^* is nearly two orders of magnitude less than the free electron mass, so that operation at high frequencies is possible with only moderate applied fields. For example, a 5-kOe field will produce oscillations at 1000 GHz in the fundamental cyclotron mode.

A proposed solid state gyrotron geometry is shown in Fig. 1. It consists of a metallized cylindrical piece of indium antimonide (InSb) which forms a high-Q electromagnetic cavity. Electrons are injected into the semiconductor via a Schottky barrier. A shallow implanted layer is used to achieve the proper current characteristics. A nonaxial magnetic bias field is also provided.[†]

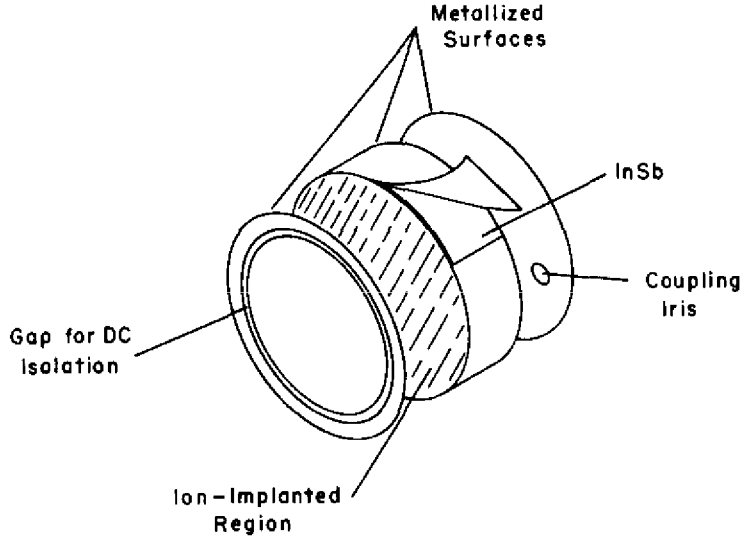

Fig. 1 — Solid state gyrotron

Manuscript submitted April 16, 1980.

[†]Detailed calculations have been carried out only for an axial magnetic bias field and a nonaxially injected electron beam. The Fig. 1 geometry is simpler to implement and the mathematical results for this case are expected to be similar to the axial bias case.

The following section reviews the physical mechanism giving rise to the oscillations and also gives the principal results of Ref. 1. The next two sections examine basic physical limitations on solid state gyrotron performance imposed by present materials and fabrication technology. Characteristics of electron injection by a Schottky barrier are discussed in the fifth section.

LINEAR THEORY

Physical Mechanism

The effective mass of an electron in the lowest conduction band in InSb is given by [1]

$$m^* = m_0^* \left[1 - \frac{V^2}{V_g^2}\right]^{-1/2} = \gamma\, m_0, \tag{1}$$

where V is the velocity of the electron, m_0^* the effective mass at the bottom of the band, and $V_g = (E_g/2\, m_0^*)^{1/2}$, where E_g is the bandgap. The electron cyclotron maser instability occurs because the cyclotron frequency $\Omega = eB_0/m^*$ $(= eB_0/\gamma m_0^* = \Omega_0/\gamma)$ depends on the energy of the electrons. Physical insight into the mechanism of this instability may be gained by considering the particle trajectories [3] shown in Fig. 2a and 2b. Electrons injected at an angle to a uniform and constant magnetic field $B_0\, \hat{e}_z$ move in helical trajectories. Figure 2a is a projection of these trajectories on the $\hat{e}_x$, $\hat{e}_y$ plane. Initially, the electrons are uniformly distributed along a cyclotron orbit. The initial radius of the electron orbit is the Larmor radius

$$r_{0L} = v_{0\perp}/(\Omega_0/\gamma_0) \quad \text{where } \gamma_0 = \left\{1 - \frac{v_{0z}^2 + v_{0\perp}^2}{V_g^2}\right\}^{-1/2},$$

$v_{0\perp}$ and v_{0z} being the initial perpendicular and parallel velocity components. A small-amplitude RF electric field $E_y(t) = \hat{e}_y\, E_0 \cos \omega_0 t$ will slightly perturb the orbits. We first examine the case when $\omega_0 = \Omega_0/\gamma_0$. The rate of change of the particle energy is $dW_b/dt = e v_y(t) E_y(t)$. With the initial choice of field direction shown in Fig. 2a, the particles in the upper half-plane lose energy. Since γ decreases, the cyclotron frequency $\Omega = \Omega_0/\gamma$ of these particles increases and the Larmor radius $r_L = v_\perp/\Omega$ decreases. The particles spiral inward and their phase tends to slip ahead of the wave. On the other hand, the particles in the lower half-plane gain energy. Their cyclotron frequency decreases and they spiral outward. The phases of these particles slip behind the wave. After a number of gyro orbits, the particles become bunched in the upper half-plane. If ω_0 is slightly greater than Ω_0/γ_0, then a net decrease in the energy of the electrons is obtained. When $\omega_0 \gtrsim \Omega_0/\gamma_0$, the electrons on the average traverse a coordinate space angle less than 2π in a wave period $2\pi/\omega_0$. All the particles then slip behind the wave and become bunched in the upper half-plane as shown in Fig. 2b. As the net kinetic energy of the particles decreases, the amplitude of the RF field increases due to conservation of energy. Depending on the initial beam parameters, the group of bunched electrons may continue to slip behind the wave or initially slip behind, reverse itself, and begin to oscillate about the positive y-axis. In any case, the bunched particles will eventually appear in the lower half-plane. The particles then gain energy and the wave amplitude decreases. The electrons have to be taken out of the cavity before this happens.

A nonlinear analysis [4] of the electron trajectories in an "empty" cavity shows that appreciable electron bunching occurs after the electrons traverse about 10 gyro orbits. In InSb at 77 K, $m_0^* = 0.014\, m_e$ (m_e = free electron mass) and $V_g = 1.3 \times 10^6$ m/s. For electron velocity of the order of 10^6 m/s, the Larmor radius ($r_L = v_\perp/\Omega$) and the pitch of the spiral trajectories ($\lambda_c = 2\pi\, v_z/\Omega$) are of the order of 0.1 and 1 mm, respectively, for a magnetic field $H_0 \cong 5$ kOe ($\Omega_0/2\pi \cong 1000$ GHz). Hence, a length of the order of 10 μm is required for electron bunching in InSb.

So far we have assumed that the electrons suffer no collisions in their trajectories. However, in solids collision is a serious obstacle to the phase bunching needed to obtain coherent radiation. The

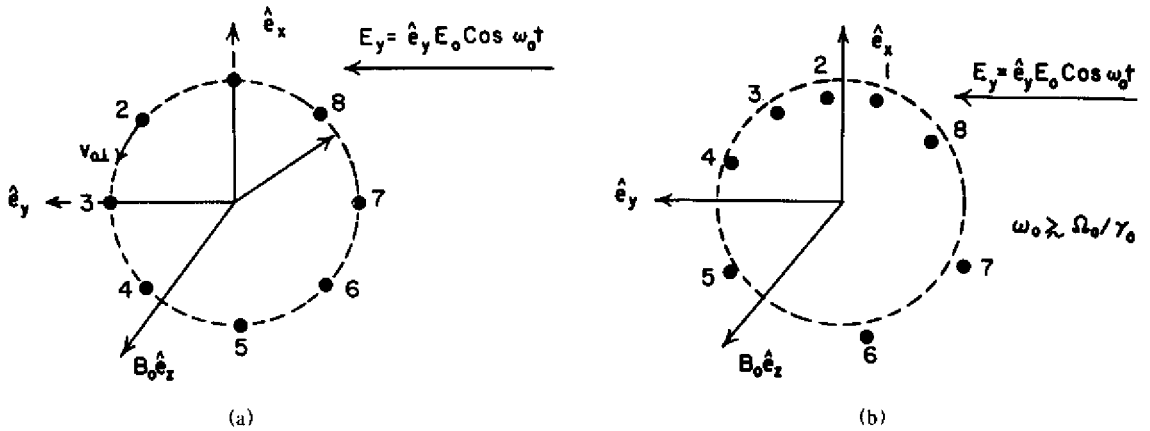

Fig. 2 — The mechanism responsible for the electron cyclotron maser illustrated by orbits of test particles in velocity space in the presence of a small external field: (a) Initial particle positions, (b) Bunched particles after several cycles [3]

electrons will remain in orbit for a distance close to the mean-free path ℓ. Conditions for cyclotron-maser interaction rapidly deteriorate when the interaction length goes much beyond ℓ. In this regard, a solid state cyclotron maser in the cavity configuration is expected to offer an advantage over a waveguide configuration because the cavity configuration requires a shorter interaction length. In the waveguide case, the beam interacts with an electromagnetic wave that grows from the noise or near-noise level, whereas in the cavity the beam interacts with a large-amplitude standing wave, which has been built up and stored in the cavity. As a result, the interaction is much stronger in the latter case and the interaction length required for the beam to lose the same amount energy becomes shorter. From the discussion in the previous paragraph, it is apparent that ℓ in InSb should not be less than 10 μm for efficient interaction at 1000 GHz, varying inversely as the frequency.

Beam Power Gain and Threshold Power

The time-average power gain P for all the electrons in a cylindrical cavity (radius R and length L) was obtained in Ref. 1 from a linear theory by solving the Vlasov equation while collisions were treated in an approximate way. For a monoenergetic beam of electrons with guiding centers distributed uniformly on a cylinder of radius r_0, P is given by

$$P = \frac{N L e^2 E_{\theta_0}^2}{8 m_0^* \gamma_0 \omega} (\alpha_1 + \alpha_2 + \alpha_3 + \alpha_4), \tag{2}$$

where N is the number of electrons per unit length, E_{θ_0} is the amplitude of the cavity field, and

$$\omega = \frac{1}{\sqrt{\mu\epsilon}} (k_n^2 + k_z^2),$$

the frequency of TE_{0nm} modes. k_n is given by the nth nonvanishing root of $J_1(k_n R) = 0$ and $k_z = m\pi/L$, μ is the permeability, and ϵ the dielectric constant. $c_0 = (\mu_0\epsilon_0)^{-1/2}$ is the velocity of light in vacuum. The quantities α_i are given by

$$\alpha_1 = -\frac{H_1(k_n r_0, k_n r_L)\, \beta_{\perp 0}^2}{\beta_g^2 \Delta} \left[\Delta_0 \left(N(\Delta) + \frac{M(\Delta)}{\Delta} \right) - \frac{k_z L \beta_g^2 \Delta}{\beta_z^2} N(\Delta) \right]$$
$$+ \frac{Q_1(k_n r_0, k_n r_2)}{\Delta} (\omega - k_z v_{z0}) \frac{L}{v_{z0}} M(\Delta) \tag{3}$$

and

$$\alpha_2 = \frac{H_1(k_n r_0, k_n r_L)\beta_{\perp 0}^2}{\beta_g^2 \Delta}\left[\Delta_0\left[N(\Delta') + \frac{M(\Delta')}{\Delta} - \frac{\Gamma}{\Delta}\right] - \frac{k_z L \beta_g^2 \Delta N(\Delta')}{\beta_z^2}\right]$$
$$- \frac{Q_1(k_n r_0, k_n r_L)}{\Delta}(\omega - k_z v_{z0})\frac{L}{v_{z0}}[M(\Delta') - \Gamma], \tag{4}$$

with

$$M(X) = \{x(1 - e^{-L/\ell}\cos x) - (L/\lambda)\, e^{-L/\ell}\sin x\}/(x^2 + L^2/\ell^2) \tag{5}$$

$$N(x) = \mathrm{Re}\left[\frac{1 - e^{(ix - L/\ell)}}{(x + iL/\ell)^2} + \frac{i\, e^{(ix - L/\ell)}}{x + iL/\ell}\right] \tag{6}$$

$$\Gamma = 2k_z L\,(1 - e^{-L/\ell})\,/\,(4k_z^2 L^2 + L^2/\ell^2)\,.$$

α_3 and α_4 are, respectively, obtained from α_1 and α_2 with the following substitutions

$$\omega = -\omega$$
$$\Delta = -\Delta'$$
$$\Delta' = -\Delta\,.$$

In Eqs. (3) through (7), we have used the following notation:

$$\beta_{\perp 0} = v_{\perp 0},\ \beta_{z0} = v_{z0}/c_0,\ \beta_g = v_g/c_0$$
$$\gamma_0 = [1 - (\beta_{\perp 0}^2 + \beta_{z0}^2)/\beta_g^2]^{-1/2},$$
$$\Delta_0 = (\omega^2 - K_z^2\beta_g^2 c^2)L^2/v_{z0}^2,$$
$$\Delta = (\omega - K_z v_{z0} - \Omega_0/\gamma_0)L/v_{z0},$$
$$\Delta' = (\omega + K_z v_{z0} - \Omega_0/\gamma_0)L/v_{z0}.$$

The functions $H_1(a_1,a_L)$ and $Q_1(a_0,a_L)$ in Eqs. (3) and (4) are defined by

$$H_1(a_0,a_L) = \{J_1'(a_L)\, J_1(a_0)\}^2$$
$$Q_1(a_0,a_L) = 2H_1(a_0,a_L) + a_L J_1''(a_L)\, J_1'(a_L)\, J_1^2(a_0) \tag{8}$$
$$+ \frac{1}{2}\, a_L J_1'(a_L)\,\{J_0^2(a_0)J_0'(a_L) - J_2^2(a_0)J_2'(a_L)\}\,.$$

The modification in a when the beam is not monoenergetic will be discussed in the fourth section.

From the conservation of total energy, the rate of increase of the stored electromagnetic energy W_f in the cavity is equal to the rate of loss of the electron beam energy. Thus,

$$\frac{dW_f}{dt} = -P$$
$$= -\frac{N e^2}{\pi R^2 \epsilon m_0^*}\,\frac{\alpha}{2\gamma_0 \omega J_0^2(k_n R)}\, W_f, \tag{9}$$

where

$$W_f = \frac{\pi}{4}\, R^2 L\, \epsilon J_0^2\,(k_n R)\, E_{\theta_0}^2. \tag{10}$$

For the perturbation theory to be valid, the quantity $J = -Ne^2\alpha/2\pi R^2\, \epsilon m_0^*\, \gamma_0 \omega J_0^2\,(k_n R)$ should be less than 1. This condition sets an upper limit on the value of N.

A plot of $<\alpha>$ as a function of $\bar{f} - \bar{f}_H$ for different values of L/ℓ is shown in Fig. 3. The dimensionless quantities $\bar{f}$ and $\bar{f}_H$ are defined, respectively, by

$$\bar{f} = \frac{1}{2\pi} \frac{\omega R}{c_0}$$

and

$$\bar{f}_H = \frac{1}{2\pi} \frac{\Omega_0}{\gamma_0} \frac{R}{c_0}.$$

The wave amplitude increases when $<\alpha>$ is negative; α becomes negative for $\bar{f} - \bar{f}_H$ in the range $0 < \bar{f} - \bar{f}_H < 0.015$. The maximum negative value of $<\alpha>$ occurs around $\bar{f} - \bar{f}_H \cong 0.0055$. The magnitude of $<\alpha>$ decreases rapidly with increase in L/ℓ.

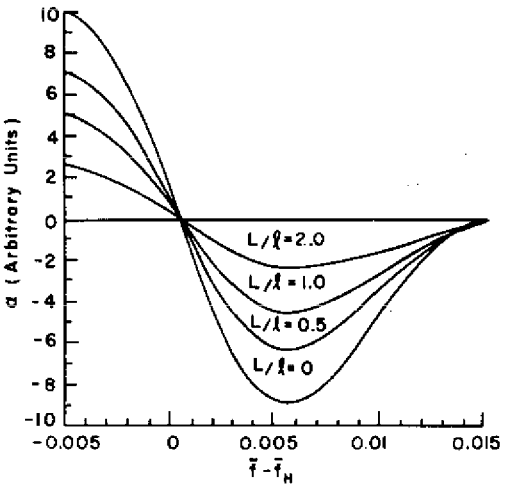

Fig. 3 — Gain α vs synchronism parameter $(\bar{f} - \bar{f}_h)$ for $n = m = 1$, $\Omega_0 = 0.48$, $\gamma_0 = 1.1$, $L/R = 0.1$, $\beta_{\perp 0}/\beta_{z0} = 1.5$, and four different values of L/ℓ. The relative dielectric constant is 17.7.

A general requirement for oscillations in a cavity of finite Q is given by

$$-P \geqslant \frac{\omega W_f}{Q}. \tag{11}$$

The kinetic energy W_b of the electrons in the conduction band may be written as [1]

$$W_b = (\gamma_0 - 1)\, m_0^* v_g^2, \tag{12}$$

and the electron beam power P_b in the crystal is

$$P_b = N(\gamma_0 - 1)\, m_0^* v_g^2 v_{0z}. \tag{13}$$

From Eqs. (2), (11), and (13), the threshold beam power P_b^{th}

$$P_b^{th} = -\left(\frac{\omega R}{c_0}\right)^2 \cdot \frac{\gamma_0(\gamma_{0-1})\beta_g^2 \beta_{0z} J_0^2(k_n R)}{\alpha Q} \cdot \frac{4\pi \epsilon m_0^* c_0^5}{2e^2}, \tag{14}$$

where $\alpha = \alpha_1 + \alpha_2 + \alpha_3 + \alpha_4$. In Fig. 4, QP_b^{th} is plotted as a function of the electron kinetic energy in the crystal $W_b = (\gamma_0 - 1) m_0^* c^2 \beta_g^2$ for cyclotron frequency Ω_0/γ corresponding to the maximum beam power loss. The threshold power increases rapidly with increase in L/ℓ The contribution to Q from various loss mechanisms will be discussed in on page 7.

The gain in energy of the cavity fields is derived from the energy of the electrons associated with their motion transverse to the direction of the applied magnetic field. This exchange of energy may be

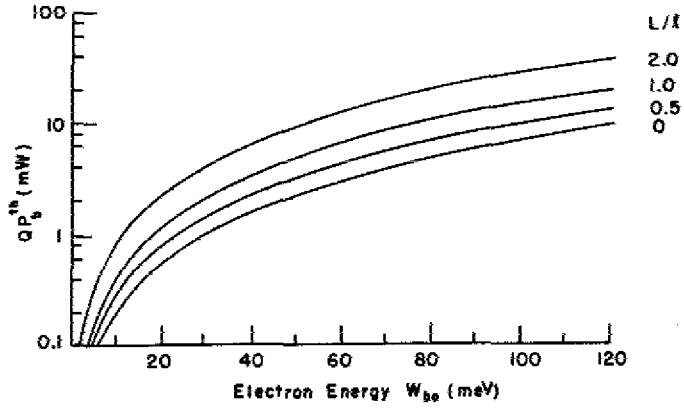

Fig. 4 — Dependence of the oscillation threshold on the electron kinetic energy W_b for four values of L/ℓ. Values assumed for other parameters are $\Omega_0 = 0.48$, $L/R = 0.1$, $\gamma_0 = 1.1$, and $\beta_{\perp 0}/\beta_{z0} = 1.5$.

explained from another point of view. In a magnetic field the energy of the transverse motion W_b of the electrons is quantized into Landau levels with $W_{b1} \cong (S + 1/2)\ \hbar\ \Omega_0/\gamma$, S being an integer. The separation between levels slowly decreases with increasing energy. The electrons are initially injected at an energy level with large S (typically $S \simeq 20$ and $\Omega_0/\gamma_0 \simeq 5$ meV). If $\omega \gtrsim \Omega_0/\gamma_0$, then there is a net downward transition of electrons due to the coupling of the electrons and the cavity fields. The electrons undergo a succession of downward transitions with $\Delta S = 1$ and emit radiation.

The electrons may also lose energy by other scattering mechanisms. Three other principal scattering processes at low temperature ($T \leqslant 77$ K) and low electron densities ($n_0 \simeq 10^{13}/\text{cm}^3$) are longitudinal optic phonon scattering, charged impurity scattering, and electron-electron collisions. Longitudinal optic phonon energy in InSb is about 24 meV. Electron-phonon interaction will involve transitions with $\Delta S \cong 5$. The transition probabilities for these three scattering mechanisms are smaller than that due to the electron-radiation interaction. Hence the loss of transverse energy of the electrons from these three scattering mechanisms is not expected to be appreciable. The longitudinal motion of the electrons will, however, be seriously affected by these collision processes and considerations of a finite mean-free path become important. Let τ_{ph}, τ_i, and τ_e denote, respectively, the mean collision time for the three scattering processes. The resultant collision time τ is given by $\tau^{-1} = \tau_{ph}^{-1} + \tau_i^{-1} + \tau_e^{-1}$. Expressions for τ_{ph}, τ_i, and τ_e as functions of temperature, impurity concentration N_D, and electron concentration are available in the reference literature [5]. At $T = 77$ K and $N_D = n = 10^{13}/\text{cm}^3$, calculated values of τ_{ph} and τ_i are, respectively, 9.3×10^{-12} s and 1.06×10^{-10} s. τ_e is of the order of 10^{-1} s. Thus, for this impurity concentration, optic phonon scattering dominates at $T = 77$ K. The experimental value of τ is found to be $\cong 6 \times 10^{-12}$ s, the mean-free path is $\ell = v_{th}\tau \cong 3\ \mu$m. As the temperature is decreased τ_{ph} increases but τ_i decreases. For this case, the resultant τ attains a maximum near $T = 32$ K. In general, an improved value of ℓ may be obtained by using highly pure InSb samples and operating at low temperatures. Finally, it should be noted that the above mean-free-path calculations strictly apply to only small deviations from thermal equilibrium. In the present solid-state gyrotron configuration, "hot" electrons in approximately a Gaussian distribution with a maximum at an energy $W_b >> kT$ are injected into the InSb sample. The mean-free path of these hot electrons might be expected to be somewhat different from that of thermal electrons. Thus the above calculations should be considered only as a guide to what could be obtained experimentally for a solid-state gyrotron.

PROPERTIES OF THE ELECTROMAGNETIC CAVITY

Quality Factor

To sustain oscillations the electron beam must supply sufficient power to overcome all sources of loss for the cavity. As was noted in Eq. (11), the threshold beam current is in fact inversely proportional to the loaded Q ($= Q_L$) of the cavity. In this section the important loss factors will be examined.

For a dielectric loaded cavity Q_L is given by the expression

$$\frac{1}{Q_L} = \frac{1}{Q_c} + \frac{1}{Q_d} + \frac{1}{Q_e}, \tag{15}$$

where Q_d accounts for losses in the dielectric material, Q_c for conductor losses in the cavity sidewalls and endwalls, and Q_e for coupling losses to the external circuitry.

For a TE_{011} mode cylindrical cavity, Q_c is given by [6]

$$Q_c\left(\frac{\delta}{\lambda_d}\right) = \frac{\left[3.8^2 + \left(\frac{\pi D}{2L}\right)^2\right]^{3/2}}{2\pi\left[3.8^2 + \left(\frac{\pi}{2}\right)^2\left(\frac{D}{L}\right)^3\right]}. \tag{16}$$

In this expression δ is the electromagnetic skin depth, λ_d the wavelength in the dielectric medium, and D and L are the cavity diameter and length, respectively. A large-diameter cavity should be used to maximize the output power; i.e., $D/L >> 1$. With this approximation Eq. (16) reduces to

$$Q_c(\delta/\lambda_d) = 1/4. \tag{17}$$

With assumed values of constants appropriate for a copper-clad InSb resonator at 77 K ($\rho_{Cu} = 0.16 \times 10^{-6}\ \Omega \cdot \text{cm}$, $\epsilon_r = 17.7$),

$$Q_c \approx 9 \times 10^8 f^{-1/2}. \tag{18}$$

Q_d is given simply by the quotient of real and imaginary portions of the dielectric constant, i.e.,

$$Q_d = \frac{\omega\epsilon}{\sigma}, \tag{19}$$

where σ is the AC conductivity. In the presence of a DC magnetic bias field,

$$\sigma = \frac{\sigma_0}{1 + (\omega - \omega_H')^2\tau_c^2}. \tag{20}$$

Here, σ_0 is the DC conductivity ($= n\ e\ \mu$), ω_H' is the cyclotron resonance frequency of the background electrons and τ_c is the cyclotron relaxation time. From Eqs. (19) and (20),

$$Q_d = \left[\frac{\omega\epsilon}{n\ e\ \mu}\right][1 + (\omega - \omega_H')^2\,\tau_c^2]. \tag{21}$$

If standard values for high-purity InSb (see Table 1) are used and if $\omega/2\pi$ is assumed to be 1000 GHz, the coefficient of the bracketed term is only ≈ 10. However, because the effective mass of the background electrons is different from that of the injected electrons, the dielectric Q can still be very large. For example, with $\tau_c = 10^{-10}$ s [8], $\omega = 2\pi \times 10^{12}$ s, and $\gamma = 1.1$, then $Q_d \cong 10^4$. Thus $Q_d >> Q_c$.

Table 1 — Properties of High-purity InSb at 77 K

Characteristic	Value	Reference
Effective mass, m_0^*	0.013 m_0	7
Bandgap, E_g	0.25 eV	5
Mobility, μ	1.1×10^6 ($n_0 = 8 \times 10^{12}$)	5
	7×10^5 ($n_0 = 1.8 \times 10^{13}$)	8
Relative dielectric constant, ϵ_r	17.0	7

Q_e can be made as large as desired by adjusting the coupling iris size. Fairly weak coupling is desired for minimum threshold, but it must be sufficiently large to couple appreciable power to the output circuitry.

Thus, metallic losses in the cavity walls dominate all other sources of loss. With careful polishing of the InSb sample and use of a high-purity copper conductor, loaded Q's $\cong$ 500 should be achievable at 1000 GHz.

Mode Density

It was noted previously that a large value of D/L is desirable to maximize the power output. This ratio cannot be increased without limit, however, since unwanted modes appear within the passband, which can result in spurious oscillations and in general a degraded spectral output. The resonant frequency of a cylindrical cavity is given by the expression [6]

$$f_R = \frac{C_d}{2L}\left[n^2 + \left(\frac{X_{\ell m}}{\pi}\right)^2 \left(\frac{L}{R}\right)^2\right]^{1/2}, \tag{22}$$

where n is an integer, $X_{\ell m}$ is the mth root of $J_\ell(x) = 0$ for TE modes, and the m th root of $J_\ell(x) = 0$ for TM modes. c_d is the electromagnetic wave velocity in the dielectric medium. Table 2 indicates the normalized resonance frequency f_R/f_0, $f_0 = c_d/2L$ for two values of L/R. Note that for $L/R = 0.1$ and $Q = 500$, only one mode other than the desired TE_{021} mode will occur within the cavity passband. When the cavity radius is doubled, i.e., $L/R = 0.05$, the TE_{211} and TE_{311} modes also appear within the TE_{011} passband. All modes have approximately the same Q, but some mode selectivity is possible through proper location of the coupling iris. A further reduction in L/R will result in a very crowded modal spectrum within the TE_{011} passband; thus it is desirable to maintain $L/R \geqslant 0.05$ to assure a clean response.

ELECTRON BEAM REQUIREMENTS

Threshold Current Density

The current density necessary to sustain oscillations can be determined from the threshold condition (Eq. (11)). For $n = 1$ and $R/L >> 1$ this expression may be written

$$NQ_L \geqslant 2\pi^3 \left(\frac{R}{L}\right)^2 J_0^2(k_n R)\, \frac{m_0^* c^2 \epsilon_0}{e^2}\, \frac{\gamma_0}{\alpha}. \tag{23}$$

Table 2 — Mode Density of a Cylindrical Cavity
Normalized Resonant Frequency, f_R/f_0

Mode	$L/R = 0.1$	$L/R = 0.05$
TE_{111}	1.0017	1.0004
TE_{011}	1.0029	1.0007
TE_{211}	1.0047	1.0012
TE_{111}, TE_{011}	1.0074	1.0019
TE_{311}	1.0089	1.0022
TM_{211}	1.0133	1.0033
TE_{411}	1.0142	1.0036
TE_{121}	1.0143	1.0036
TM_{021}	1.0153	1.0039
TM_{311}	1.0204	1.0051
TE_{511}	1.0206	1.0052
TE_{211}	1.0225	1.0057
TM_{121} TE_{021}	1.0246	1.0068

With use of values appropriate for a TE_{011} cavity and material constants for InSb given in Table 1, the threshold condition simplifies to

$$NQ_L \geqslant (5 \times 10^{10}) \frac{\gamma_0}{\alpha} \frac{R^2}{L^2} \text{ per cm.} \tag{24}$$

The line density N can be converted to a volume charge density n by

$$n = \frac{N}{\pi R^2 \beta}, \tag{25}$$

where β is the fraction of the cavity endwall covered by the injected beam. The current density J is given by

$$J = ne\, v_{0z}. \tag{26}$$

Examination of the expressions for the driving terms of the oscillation [1] shows that the maximum filling factor obtainable is $\approx$ 20%. Combining Eqs. (23) through (26) and using this approximation lead to the following expression for the oscillation threshold:

$$J_{th} = (1.3 \times 10^{-8}) \frac{v_{0z}}{L^2 Q_L} \frac{\gamma_0}{\alpha}. \tag{27}$$

For the $L/\lambda = 0$ case shown in Fig. 3, J is only 0.034 A/cm^2. However, this is a low electron energy case ($W_b = 12$ meV). The threshold increases rapidly with increasing electron energy, decreasing mean-free path (see Fig. 4), and with energy spread, to be discussed in the next section.

Thermal Spread

The beam power gain P in Eq. (2) is derived for a monoenergetic beam of electrons injected at a constant angle to the uniform magnetic field. In any practical injection scheme, there may be a spread in both energy and angle. As shown in Fig. (2), P depends sensitively on the factor $\omega + k_z v_z - \Omega_0/\gamma$.

A spread in the initial values of v_z and $v_\perp$ will alter the beam power gain. The linear theory can be generalized to include any arbitrary electron distribution function in the momentum space. Numerical calculations are considerably simplified in the following two cases: (a) spread in the magnitude of the velocity but not in angle, and (b) spread in the angle but not in the magnitude of the velocity. Case (a) is appropriate for the injection scheme to be discussed in the following section. In this scheme, the initial distribution of energy is approximately Gaussian, so we assume an initial momentum space distribution function $f_0(\bar{p})$ of the form

$$f_0(\bar{p}) = \frac{C}{p_\perp}\, e^{-(p_\perp^2 + p_z^2 - p_0^2)/\bar{\Delta}^2}\, \delta(p_\perp - \eta p_z), \tag{28}$$

where $p_0^2 = p_{\perp 0}^2 + p_{z0}^2$, $\eta = p_{\perp 0}/p_{z0}$, and $\bar{\Delta}$ is the half-width. The constant C is to be determined by the normalizing condition

$$\int f_0(\bar{p})\, 2\pi\, p_\perp\, dp_\perp\, dp_z = 1. \tag{29}$$

For this distribution function, the beam power gain P and the threshold beam power P_b^{th} to sustain oscillations are, respectively, found to be

$$P = \frac{Ne^2 L\, E_{\theta_0}^2}{8\, m_0^*\, \gamma_0 \omega} \int_{-1/\theta}^{\infty} \frac{\gamma_0}{\gamma(\xi)} \left\{ \sum_{i=1}^{4} \alpha_i\, (\beta_z(\xi), \beta_\perp(\xi)) \right\} \frac{e^{-\xi^2}}{\left\{\eta^2 - \xi^2\theta^2 - 2\xi\theta\right\}^{1/2}}\, d\xi$$

$$= \frac{Ne^2 L\, E_{\theta_0}^2}{8 m_0^*\, \gamma_0 \omega} < \alpha > \tag{30}$$

and

$$P_b^{th} = -\left(\frac{\omega R}{c}\right)^2 \frac{4\pi \epsilon m_0^{*2}\, c^5 \gamma_0 \beta_g^2 J_0^2(x_n)}{2e^2 < \alpha > Q} \int_{-1/\theta}^{\infty} (\gamma(\xi) - 1)\beta_z(\xi) \frac{e^{-\xi^2}\, d\xi}{\left\{\eta^2 - \xi^2\theta^2 - 2\xi\theta\right\}^{1/2}}, \tag{31}$$

where

$$\theta = \bar{\Delta}^2/p_0^2 \cong \Delta W_b/W_{b0},$$

$$W_{b0} = (\gamma_0 - 1)\, m_0^* v_g^2$$

$$\gamma_0 = \left[1 - \frac{v_{0z}^2 + v_{\perp 0}^2}{v_g^2}\right]^{-1/2},$$

$$\gamma(\xi) = \left[1 + \eta^2 \gamma_0^2 \frac{\beta_{0z}^2}{\beta_g^2}\, (1 + \xi\theta)\right]^{1/2},$$

$$\beta_z(\xi) = \beta_{0z} \frac{\gamma_0}{\gamma(\xi)}\, (1 + \xi\theta)^{1/2}, \tag{32}$$

$$\beta_\perp(\xi) = \eta \beta_z(\xi),$$

and α_i's are obtained from Eqs. (3)—(7), replacing $\beta_{\perp 0}$ and β_{0z} by $\beta_\perp(\xi)$ and $\beta_z(\xi)$, respectively. The integrations in Eqs. (30) and (31) are to be performed numerically. The values of $< \alpha >$ as a function of the parameter $\bar{f} - \bar{f}_H$ are shown in Fig. 5 for different values of $\Delta W_b/W_{b0}$. $< \alpha >$ decreases rapidly with increases in thermal spread and the value of $\bar{f} - \bar{f}_H$ corresponding to the maximum negative value of $< \alpha >$ shifts to higher values (i.e., smaller magnetic fields at a given frequency). The decrease in $< \alpha >$ will increase the threshold power as $\Delta W/W_b$ increases. This is shown in Fig. 6 where QP_b^{th} is plotted as a function of W_{b0} for different values of $\Delta W/W_{b0}$. The threshold current density (Eq. (27)) is shown in Fig. 7 for this same case.

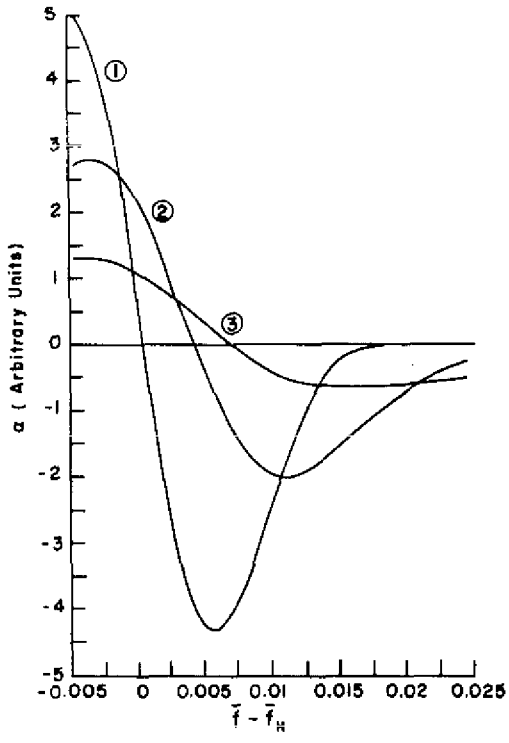

Fig. 5 — $<\alpha>$ as a function of $(\bar{f}-\bar{f}_h)$ for three different values of energy spread: (1) $\Delta W_b/W_{b0} = 0$, (2) $\Delta W_b/W_{b0} = 0.1$ and (3) $\Delta W_b/W_{b0} = 0.2$. Other parameters assumed are $n = s = m = 1$, $r_0 = 0.48R$, $L/R = 0.1$, $L/\ell = 1.0$, and $\beta_{\perp 0}/\beta_{z0} = 1.5$.

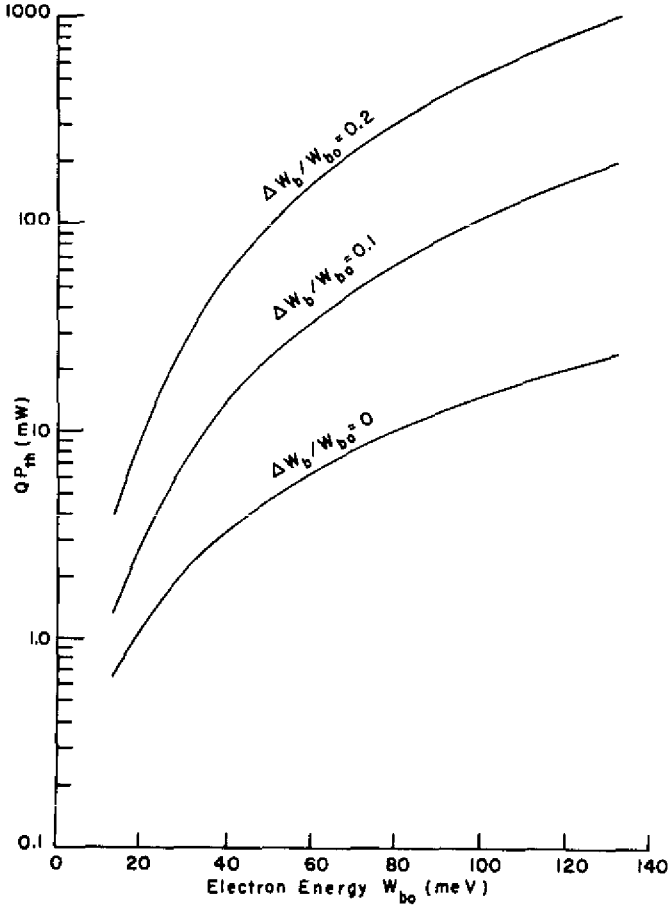

Fig. 6 — Threshold power as a function of beam kinetic energy $\bar{W}_{b0}$ at different values of $\Delta\bar{W}/\bar{W}_{b0}$. The magnetic field is chosen corresponding to the maximum beam energy loss. Other parameters are the same as in Fig. 5.

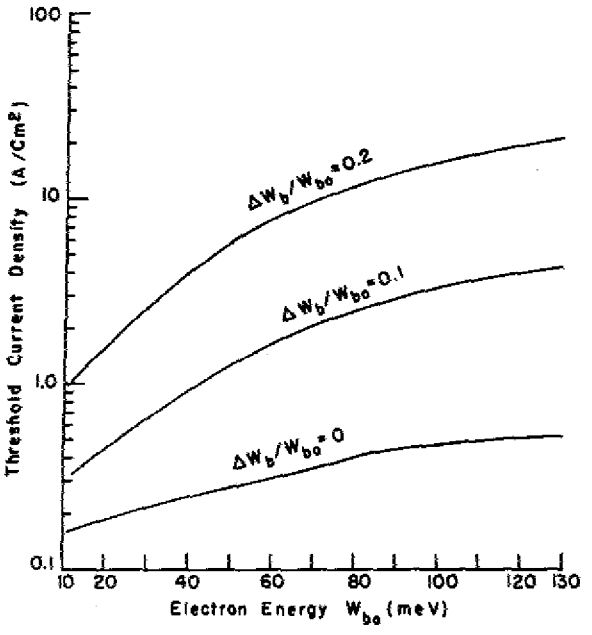

Fig. 7 — Threshold current density as a function of kinetic energy W_{b0}. Parameters are the same as in Figs. 5 and 6.

ELECTRON INJECTION VIA SCHOTTKY BARRIERS

Introduction

In the tube gyrotron, electrons are injected into the interaction region in an annular beam from a specially designed electron gun. This is not an attractive approach for the solid-state gyrotron because of its complexity, as electrons must be injected in a vacuum at 77 K in the presence of a DC magnetic field. A more fundamental reason for not employing electron gun injection is that when electrons are injected into the conduction band of a semiconductor from vacuum they gain an amount of energy equivalent to the semiconductor's electron affinity, which for InSb is $\approx$ 4 eV. Since the bandgap is only 0.24 eV, the electrons will immediately thermalize by exciting electron-hole pairs. It will thus be impossible to maintain a proper electron energy distribution for sustaining oscillations. This problem can be circumvented only if the InSb surface can be treated in such a way as to reduce the electron affinity to near zero. Such techniques have been reported for GaAs but not for InSb [9].

A solid state electron injection approach is thus preferable. This approach must be capable of providing current density of $\gtrsim$ 1 A/cm^2 with an energy spread of $\lesssim$ 20 meV. The dependence of threshold upon the thermal spread inherent in the injection process was discussed in the previous section. A further restriction on the injection geometry is that only small electric fields can be tolerated within the interaction region. In particular an electric field E will result in an energy spread ΔW_b if the interaction region is one mean-free-path long, where

$$\Delta W_b = Ee\ell. \tag{33}$$

Thus $\Delta W_b \leqslant 10$ meV requires $E \leqslant 10$ V/cm for $\ell = 10\ \mu$m. This consideration alone is sufficient to rule out Read-diode and simple ohmic injection.

The ideal injecting structure is indicated in Fig. 8. The electrons are injected by a metal electrode, accelerated in a high-field region, and interact with the cavity fields within the distance ℓ where no electric field is present.

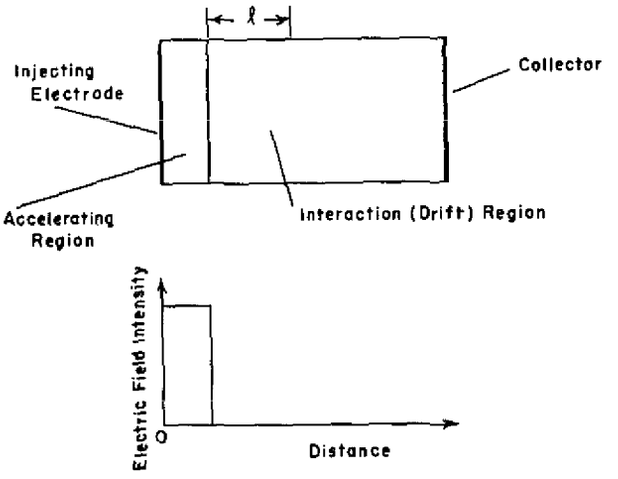

Fig. 8 — Ideal solid-state injection geometry and electric field profile

This can be approximated by a Schottky tunnel barrier configuration, as is shown in Fig. 9. It consists of an intrinsic, high-mobility semiconductor which has a shallow implanted or epitaxial region. Electrons are injected into the interaction region ℓ by tunneling through the Schottky barrier. The i-region is not depleted; hence, $E = 0$ within the interaction region as required. The electron velocity distribution is determined by the carrier concentration within the n region and by the applied bias voltage, as discussed in the following section.

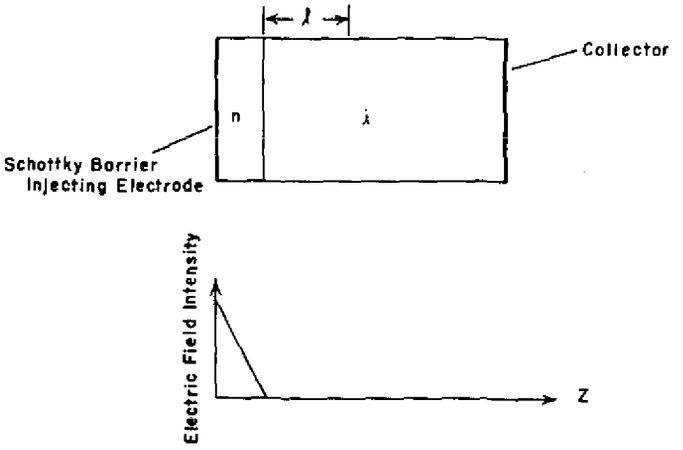

Fig. 9 — Schottky barrier injection geometry and electric field profile

Analysis

A number of excellent analyses of tunneling currents through Schottky barriers have been reported [10,11]. We will follow the work of Crowell and Rideout [11], since their approach is fairly simple to employ and is applicable to the low doping levels which we require. Padovani and Stratton [10] employ a similar approach, but their work is more applicable to high doping densities. Starting with the one-dimensional, time-independent WKB transmission probability through a barrier, Crowell and Rideout show that the normalized forward current density, if through a Schottky barrier, is

$$\frac{I_f}{I_m} = \frac{E_b}{kT} \int_0^1 e^{-\frac{E_b}{kT}\left[\alpha + \frac{kT}{E_{00}} y(\alpha)\right]} d\alpha + e^{-\frac{E_b}{kT}}, \tag{34}$$

where

$$\alpha = E/E_b,$$

$$y(\alpha) = (1-\alpha)^{1/2} - \alpha \ln \frac{[1+(1-\alpha)^{1/2}]}{\alpha^{1/2}}$$

$$I_m = A^* T^2 e^{-q\phi_s/kT},$$

$$E_{00} = \frac{eh}{4\pi}\left[\frac{n}{m^*\epsilon}\right]^{1/2}.$$

In these expressions, A^* = Richardson constant, E = electron energy, E_b = band bending at the semiconductor—metal interface, and ϕ_s is the Fermi energy in the semiconductor. These quantities are illustrated in Fig. 10. The reverse current density I_r is related to the forward current density by

$$I_r = I_f\, e^{-eV_f/kT}, \tag{35}$$

where V_f is the applied forward voltage.

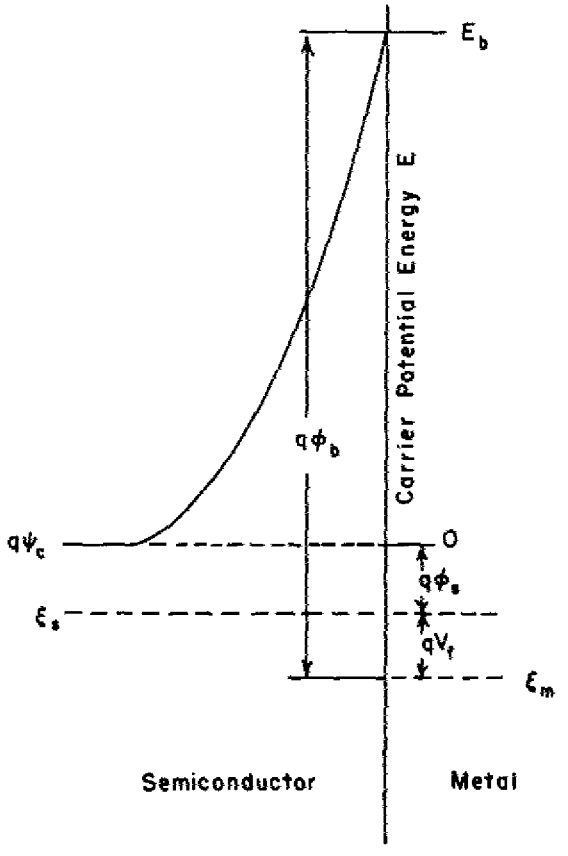

Fig. 10 — Potential energy vs distance for carriers in a forward-biased metal-semiconductor (Schottky) barrier (after Crowell and Rideout [11])

The two quantities of primary concern for the solid state gyrotron are the energy spread of the electrons and the current density. The electron density is peaked about an energy E_m, where

$$\frac{E_m}{E_b} = \left[\cosh \frac{E_{00}}{kT}\right]^{-2}. \tag{36}$$

For high doping densities $kT/E_{00} \leqslant 1$ ($n \gtrsim 10^{16}/\text{cm}^3$ for InSb at 77 K), field emission is dominant, whereas for $kT/E_{00} \geqslant 1$, thermonic emission is dominant. The percentage energy spread can be calculated from the integrand of Eq. (34). It is a sensitive function of the properties of the semiconductor and the applied bias voltage, ranging from less than 10% to more than 100%.

Crowell and Rideout [11] show that the reverse-current density can be written as

$$I_r = \left(\frac{I_{ma}}{I_m}\right) A^* T^2 \, e^{-q\phi_b/kT} \, e^{-\frac{E_b}{kT}(1-1/n)}. \tag{37}$$

The quantities I_{ma}/I_m and n are given in Figs. 6 and 7 of Ref. 8 and are reproduced here in Figs. 11 and 12. The barrier height ϕ_b is 53 meV for InSb at 77 K, so Eq. (37) becomes

$$I_r = 3.4 \left(\frac{I_{ma}}{I_m}\right) e^{\frac{E_b}{kT}(1-1/n)}. \tag{38}$$

Calculations for some cases of interest are shown in Fig. 13. Current density and energy spread are plotted as a function of frequency for InSb carrier densities of $10^{16}/\text{cm}^3$, $10^{15}/\text{cm}^3$, and $<< 10^{15}/\text{cm}^3$ (thermionic limit). A comparison of these curves with the threshold current curves (Fig. 7) shows that, for electron energies exceeding 60 meV for the $n = 10^{15}/\text{cm}^3$ case and 100 meV for the thermonic limit case, the Schottky barrier can supply sufficient current to exceed the threshold.

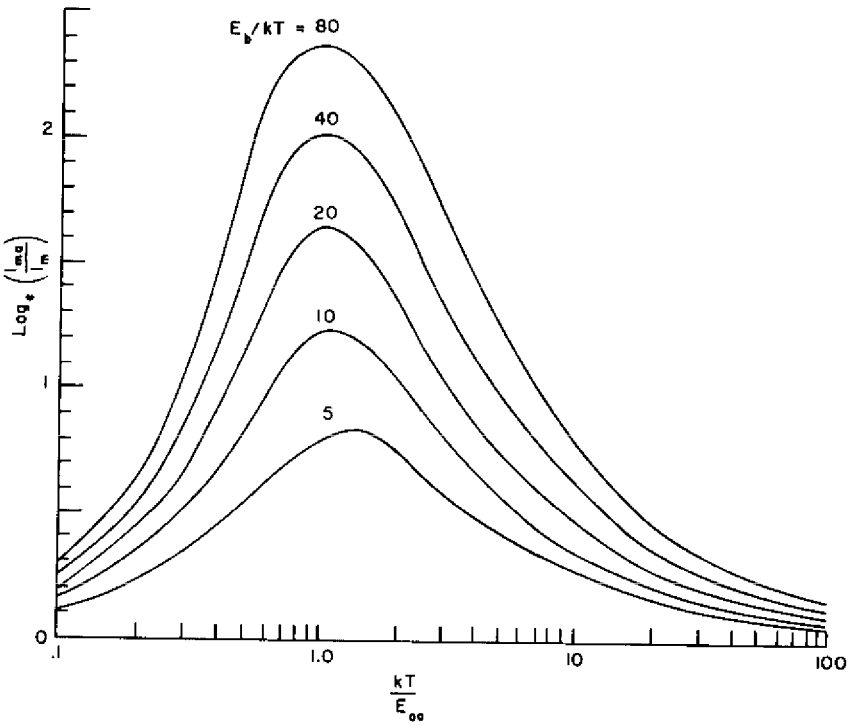

Fig. 11 — Normalized apparent saturation current density vs kT/E_{00} for selected values of E_b/kT (after Crowell and Rideout [11])

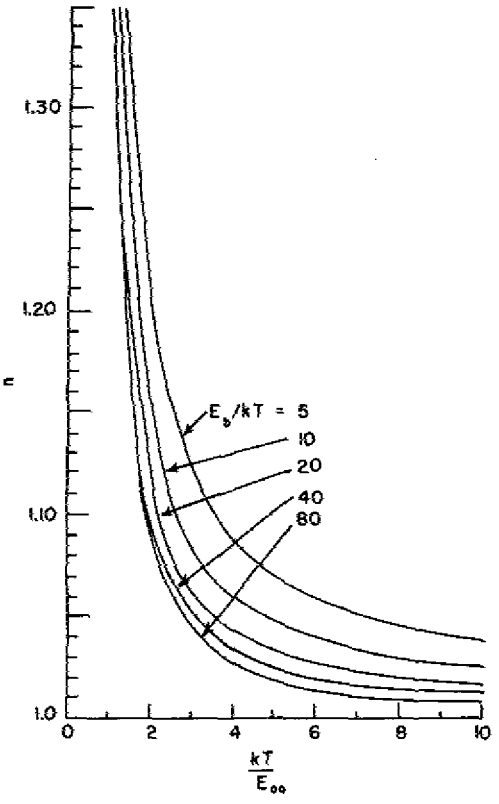

Fig. 12 — Diode n vs kT/E_{00} for selected values of E_b/kT (after Crowell and Rideout [11])

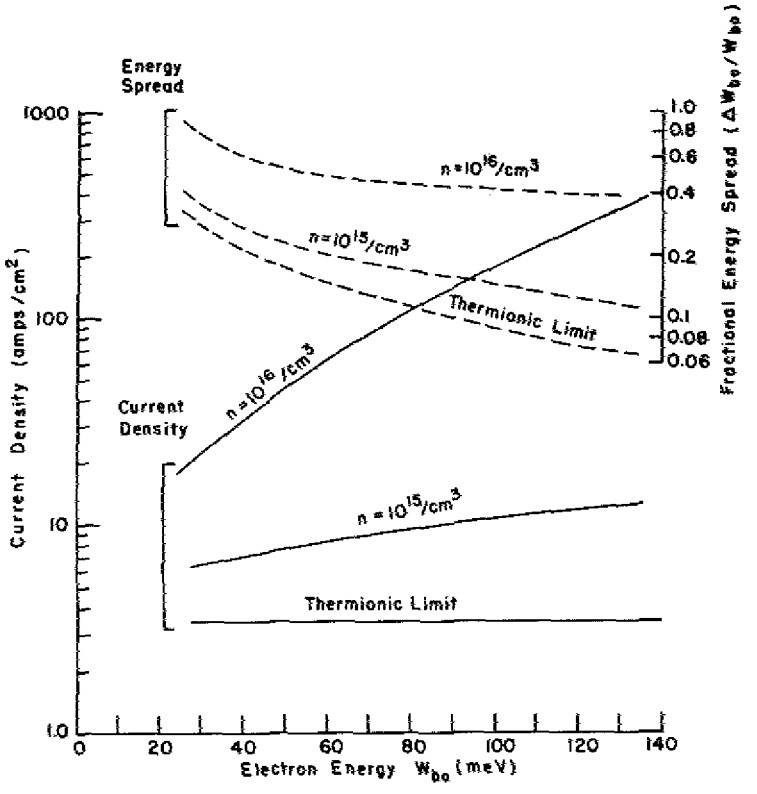

Fig. 13 — Theoretical current density and energy spread as a function of electron energy for a reverse-biased Au-InSb Schottky barrier with selected carrier concentrations

In summary, the Schottky-barrier tunnel junction appears capable of supplying current densities sufficiently large to sustain oscillations if the electron mean-free path is comparable to the cavity length.

SUMMARY AND CONCLUSIONS

A geometry for realizing solid-state gyrotron oscillation has been analyzed in detail. Cavity loss mechanisms and electron beam requirements were examined. Previous theoretical work was modified to include the effects of a thermal spread in electron energy upon the oscillation threshold. It was shown that, by injecting electrons via a Schottky tunnel barrier, the current density would be sufficient to sustain oscillations if the mean-free path is comparable to the cavity length.

Throughout this report it has been stressed that the key to realizing a successfully operating device is a long mean-free path ℓ. It was pointed out that ℓ must be about 10 μm long to obtain substantial electron bunching and thus reasonable efficiency. Furthermore, the oscillation threshold increases rapidly with decreasing ℓ (Fig. 4). At the present time the maximum mean-free path reported in the literature is about 3 μm (InSb at 77 K). However, higher values do appear feasible [13]. Considering the uncertainties inherent in the analysis and the proximity of existing and projected materials properties to calculated requirements, an experimental feasibility program seems warranted.

Such an experimental program has been initiated at NRL. The first phase entails development of the technologies required to fabricate the solid-state gyrotron structure. This includes ion-implantation and Schottky-barrier development, technologies which are currently not well established for InSb. We also plan to initiate a program to obtain higher purity samples of InSb. With progress in these areas we will be in a position to initiate experiments to establish the viability of the solid-state gyrotron as a submillimeter-wave source.

REFERENCES

1. A.K. Ganguly and K.R. Chu, *Phys. Rev.* **B18**, 6880–6889 (1978).

2. J.L. Hirshfield and V.L. Granatstein, *IEEE Trans.* MTT-25, 522 (1977).

3. P. Sprangle and A.T. Drobot, *IEEE Trans.* MTT-25, 528 (1977).

4. K.R. Chu, NRL, private communication.

5. C. Hilsum and A.C. Rose-Innes, *Semiconducting III-V Compounds*, Pergamon Press, New York, 1961, p. 179.

6. C.G. Montgomery, ed., *Technique of Microwave Measurements*, MIT Radiation Laboratory Series, McGraw-Hill, New York, 1947, pp. 297–303.

7. S.M. Sze, *Physics of Semiconductor Devices*, Wiley & Sons, New York, 1969, p. 20.

8. E. Gornik, T.Y. Chang, T.J. Bridges, V.T. Nguyen, J.D. McGee, and W. Müller, *Phys. Rev. Lett.* **40**, 1151 (1978).

9. J.E. Davey, NRL, private communication.

10. F.A. Padovani and R. Stratton, *Solid State Electron.* **9**, 695 (1966).

11. C.R. Crowell and V.L. Rideout, *Solid State Electron.* **12**, 89 (1969).

12. M. McColl and M.F. Millea, *J. Electron. Mater.* **5**, 191 (1976).

13. E.M. Swiggard, NRL, private communication.